

Visualizing supercurrents in ferromagnetic Josephson junctions with various arrangements of 0 and π segments

C. Gürlich,¹ S. Scharinger,¹ M. Weides,^{2,*} H. Kohlstedt,³
R.G. Mints,⁴ E. Goldobin,¹ D. Koelle,¹ and R. Kleiner¹

¹*Physikalisches Institut – Experimentalphysik II and Center
for Collective Quantum Phenomena, Universität Tübingen,
Auf der Morgenstelle 14, D-72076, Tübingen, Germany*

²*Institute of Solid State Research and JARA-
Fundamentals of Future Information Technology,
Research Center Jülich, D-52425 Jülich, Germany*

³*Nanoelektronik, Technische Fakultät,
Christian-Albrechts-Universität zu Kiel, D-24143 Kiel, Germany*

⁴*The Raymond and Beverly Sackler School of Physics and Astronomy,
Tel Aviv University, Tel Aviv 69978, Israel*

(Dated: March 5, 2022)

Abstract

Josephson junctions with ferromagnetic barrier can have positive or negative critical current depending on the thickness d_F of the ferromagnetic layer. Accordingly, the Josephson phase in the ground state is equal to 0 (a conventional or 0 junction) or to π (π junction). When 0 and π segments are joined to form a “0- π junction”, spontaneous supercurrents around the 0- π boundary can appear. Here we report on the visualization of supercurrents in superconductor-insulator-ferromagnet-superconductor (SIFS) junctions by low-temperature scanning electron microscopy (LTSEM). We discuss data for rectangular 0, π , 0- π , 0- π -0 and $20 \times (0-\pi-)$ junctions, disk-shaped junctions where the 0- π boundary forms a ring, and an annular junction with two 0- π boundaries. Within each 0 or π segment the critical current density is fairly homogeneous, as indicated both by measurements of the magnetic field dependence of the critical current and by LTSEM. The π parts have critical current densities j_c^π up to 35 A/cm² at $T = 4.2$ K, which is a record value for SIFS junctions with a NiCu F-layer so far. We also demonstrate that SIFS technology is capable to produce Josephson devices with a unique topology of the 0- π boundary.

PACS numbers: 74.50.+r, 85.25.Cp 74.78.Fk 68.37.Hk

*Current address: Department of Physics, University of California, Santa Barbara, CA 93106, USA

I. INTRODUCTION

As predicted more than 30 years ago[1], Josephson junctions can have a phase drop of π in the ground state. Such π junctions are now intensively investigated, as they have a great potential for applications in a broad range of devices ranging from classical digital circuits[2, 3, 4, 5] to quantum bits[6, 7, 8, 9]. Nowadays, π Josephson junctions can be fabricated by various technologies, including junctions with a ferromagnetic barrier [10, 11, 12, 13, 14, 15, 16, 17, 18], quantum dot junctions[19, 20, 21] and nonequilibrium superconductor-normal metal-superconductor Josephson junctions [22, 23, 24]

In the simplest case the supercurrent density j_s across the junctions is given by the first Josephson relation

$$j_s = j_c \sin \phi, \quad (1)$$

with the critical current density $j_c > 0$ for a 0 junction and $j_c < 0$ for a π junction. Here, ϕ is the gauge invariant phase difference of the superconducting wave function across the junction (Josephson phase).

Particularly superconductor-insulator-ferromagnet-superconductor (SIFS) junctions [11, 16, 18] are promising since, in contrast to other types of π junctions, they exhibit only small damping at low temperatures, which is necessary to study Josephson vortex dynamics as well as to use them as active elements in macroscopic quantum circuits.

Now consider a junction in the x - y plane, which has a region with critical current density $j_c^0 > 0$ (0 region) and another region having $j_c^\pi < 0$ (π region). For the sake of simplicity let us assume that the boundary between 0 and π regions runs along the y direction. When ϕ is different from 0 or π the supercurrents flow in opposite directions on the two sides of the 0- π boundary, forming a vortex, with its axis coinciding with the 0- π boundary (along the y direction), that carries a magnetic flux $\Phi = \pm\Phi_0/2$ ($\Phi_0 \approx 2.07 \times 10^{-15}$ Wb is the flux quantum) [25, 26, 27]. This is true if the junction length L in x direction is much larger than the Josephson penetration depth

$$\lambda_J = \sqrt{\frac{\Phi_0}{2\pi|j_c|\mu_0 d'}}. \quad (2)$$

Here $\mu_0 d'$ is the inductance per square (with respect to in-plane currents) of the superconducting electrodes forming the junction. For junctions having electrode thicknesses larger than the London penetration depth λ_L , $d' \approx 2\lambda_L$. Experimentally, such semifluxons have

first been studied in the context of cuprate grain boundary junctions[28, 29] or zigzag ramp junctions between Nb and YBa₂Cu₃O₇ [30]. Here, the sign change of the d -wave order parameter of the cuprates leads to the formation of 0 - π facets. In junctions with a ferromagnetic barrier the value (and the sign) of the critical current density crucially depends on the thickness d_F of the F-layer[11, 16]. A junction consisting of various 0 and π segments can, thus, be formed by selectively etching the F-layer to produce two thicknesses d_F^0 and d_F^π of the F-layer such that they correspond to critical current densities j_c^0 and j_c^π with opposite signs and $j_c^0 \approx |j_c^\pi|$ [31].

In the cuprate/Nb zigzag junctions [30, 32, 33, 34] the facets should be oriented along the crystallographic a and b axes of the cuprate electrode, imposing certain topological limitations to the 0 - π boundary. In contrast, the SIFS technology allows almost any 2D shape of the 0 - π boundary and therefore offers a higher degree of design flexibility. Below, we show an example where this boundary forms a loop. Even intersecting 0 - π boundaries should be feasible, *e.g.*, by arranging 0 and π regions in a checkerboard pattern. Unfortunately, the present SIFS technology based on a NiCu ferromagnetic layer produces a maximum $|j_c^\pi|$ which is much lower than $j_c \sim 1$ kA/cm² of standard Josephson tunnel junctions. Although j_c^π at $T = 4.2$ K has been increased from some mA/cm² for the first junctions[11], to a few A/cm² in Ref. 16 and to about 35 A/cm² in the present paper, the value of $\lambda_J \propto 1/\sqrt{|j_c^\pi|}$ is still above $50 \mu\text{m}$. Thus, the study of a multi semifluxon system would thus require unreasonably large (mm sized) junctions.

Nonetheless, also (multifacet) junctions with length $L \lesssim \lambda_J$ are interesting. For example, one can consider an array of many alternating 0 and π segments along x , where the lengths of individual segments are much smaller than λ_J . Such a structure is similar to short multifacet cuprate/Nb zigzag junctions[30, 32, 33] or high angle grain boundaries in high T_c cuprates [35] and can *e.g.* be used to realize a φ junction — a junction having a phase $\pm\varphi$ in the ground state and many other interesting properties[36, 37, 38, 39, 40].

The goal of this work is to realize Josephson junctions with various arrangements of 0 and π segments in order to demonstrate that also complex structures are feasible. We characterize these junctions by measurements of current voltage (I - V) characteristics, by $I_c(B)$ and by low-temperature scanning electron microscopy (LTSEM) [41]. By analyzing $I_c(B)$, in principle one obtains information on the supercurrent flow and (in)homogeneity of the critical current; however, the analysis at least of the more complex SIFS structures

may require to consider many unknown parameters (gradients in critical current density, local inhomogeneities etc.), making conclusions ambiguous. We thus put a strong focus on LTSEM which allows direct imaging of the supercurrent density distribution in the junctions (including counterflow areas induced by the $0-\pi$ - segments), close to I_c [34].

The paper is organized as follows. In Sec. II we discuss the sample fabrication and measurement techniques. The experimental results are presented and compared with the numerical simulations in Sec. III. Different subsections are devoted to various geometries, (0 junction for reference, $0-\pi$ and $0-\pi-0$ junctions, a junction consisting of $0-\pi$ regions periodically repeated 20 times, a disk shaped structure where the $0-\pi$ boundary forms a ring and an annular junction containing two $0-\pi$ boundaries). All investigated samples are in the short limit ($L \lesssim 4\lambda_J$). Finally, Sec. IV concludes this work.

II. SAMPLES AND MEASUREMENT TECHNIQUES

A. Sample fabrication

The Nb|Al₂O₃|Ni_{0.6}Cu_{0.4}|Nb heterostructures used for our studies were fabricated, as described in Refs. 31, 42. In brief, one starts with a Nb|Al₂O₃ bilayer (Nb thickness is 120 nm) as for usual Nb based Josephson tunnel junctions. The thicknesses of the following F-layer must be chosen very accurately to realize 0 and π regions with approximately the same critical current density. To achieve that, first the Ni_{0.6}Cu_{0.4} F-layer is sputtered onto the wafer with a thickness gradient along the y -direction to achieve a wedge-like NiCu layer. Later on, a set of structures extending along x and consisting of the $0-\pi$ devices to be measured, plus purely 0 and π reference junctions, is repeated several times along the y -direction. One of the sets will have the most suitable F-layer thickness to yield π coupling with roughly optimal critical current density. In this way the number of wafer runs which are required to get appropriate $0-\pi$ junctions is minimized. After the deposition of a 40 nm Nb cap-layer and lift-off one obtains a complete SIFS stack, however without steps in the thickness of the F-layer yet. To produce such steps, the parts of the structures that shall become π regions are protected by photo resist. Then the Nb cap-layer is removed by SF₆ reactive rf etching, leaving a homogeneous flat NiCu surface, which is then further Ar ion etched to partially remove about 1 nm of the F-layer. These areas, in the finished structures,

#	junction	facets	a (μm)	W (μm)	j_c^0 (A/cm ²)	$ j_c^\pi $ (A/cm ²)	λ_J^0 (μm)	λ_J^π (μm)	l	V_c (μV)
#1	0	1	50	10	85	-	41	-	1.2	50
#2	π	1	50	10	-	35	-	65	0.77	18
#3	0- π	2	25	10	85	35	41	65	1.0	24
#4	0- π -0	3	16.6	10	73	33	44	66	1.0	23
#5	$20 \times (0-\pi-)$	40	5	10	37	29.5	62	70	3.0	11.5
#6	0- π disk	2	9; 23.5	-	4.6	13.4	176	103	0.29	6.6
#7	0- π ring	2	310	2.5	7.3	2.5	139	239	3.5	6.8

TABLE I: Sample parameters at $T = 4.5$ K: number of facets N , facet length a , junction width W . Critical current densities j_c^0 and j_c^π for junctions #3, #4 and #5 were estimated from fits to $I_c(B)$. λ_J^0 and λ_J^π refer to the Josephson lengths of the 0 and π parts, respectively. They are calculated from Eq. (2) using the respective critical current densities j_c^0 and j_c^π . l is the normalized junction length (diameter for #6, circumference for #7), calculated from Eq. (19). The characteristic voltage $V_c = I_c^{\text{max}}/G$, where G is the junction conductance, has been inferred by fitting the I - V characteristic at maximum critical current I_c^{max} to the RSJ curve, Eq. (11). For the disk shaped 0- π junction the radius r of the inner π part and total (outer) radius R are quoted instead of a . For junction #7 the facet length a is given by half of the circumference.

realize the 0 regions, while the non-etched regions are π regions. To finish the process, after removing the photo resist, a new 40 nm Nb cap-layer is deposited and, after a few more photolithographic steps the full structures are completed having a 400 nm thick Nb wiring layer, plus contacting leads and insulating layers. The thickness of the F-layer in the devices used here is ~ 5 nm and is different for all devices as they come from different places of the chip because of a gradient in the F-layer thickness.

Several sets of 0, π , 0- π , 0- π -0 and $20 \times (0-\pi-)$ junctions were fabricated in the same technological run. The disk shaped and annular samples were fabricated during another run. Parameters of the junctions are presented in Tab. I.

B. Measurement techniques and analysis of LTSEM signal

For the measurements the samples were mounted on a LTSEM He cryostage and operated at a temperature $T \approx 4.5$ K. Low pass filters with a cutoff frequency of 12 kHz at 4.2 K, mounted directly on the LTSEM cryostage, were used in the current and voltage leads to protect the sample from external noise. Magnetic fields of up to 1.2 mT could be applied parallel to the substrate plane and thus parallel to the junction barrier layer. We recorded I - V characteristics and $I_c(B)$. To detect I_c we used a voltage criterion V_{cr} (0.2 μV for Figs. 3 and 5, 0.5 μV for Figs. 2 and 4, 1 μV for all other figures).

For selected values of magnetic field, LTSEM images were taken by recording the electron-beam-induced voltage change $\delta V(x_0, y_0)$ across the junctions (current biased slightly above I_c) as a function of the beam-spot coordinates (x_0, y_0) on the sample surface. The periodically blanked electron beam (using $f_b \approx 6.66$ kHz, acceleration voltage 10 kV, beam current 250 pA), focused onto the sample, causes local heating and thus local changes in temperature-dependent parameters like the critical current density j_c and conductivity G' of the junction. The beam current also adds to the bias current density in the beam spot around (x_0, y_0) , but for all measurements reported here the beam current density is several orders of magnitude below the typical transport current densities. Thus, this effect will be ignored here. The local temperature rise δT depends on the coordinates x , y and z . For our SIFS junctions the relevant depth z_0 is the location of the IF barrier layer, where changes in j_c and G' affect the I - V characteristics by changing the critical current I_c and the junction conductance G . We describe the temperature profile within the barrier layer of our junctions by a Gaussian distribution

$$\delta T(x - x_0, y - y_0) = \Delta T \exp \left[-\frac{(x - x_0)^2 + (y - y_0)^2}{2\sigma} \right], \quad (3)$$

where x_0 and y_0 is the position of the center of the e-beam. The LTSEM images presented below are reproduced well by simulations using $\sigma = 3.5 \mu\text{m}$; this value was used for all calculated images shown below and is somewhat larger than for other LTSEM measurements, presumably due to the relatively thick top Nb layer. Further, from the beam-induced changes δI_c of the critical current and the measured temperature coefficient dI_c/dT , we estimate $\Delta T \approx 0.5$ K. To a good approximation the beam-induced change of critical current $\delta I_c(x_0, y_0)$ is proportional to the beam-induced change of the local Josephson current

density[43], $\delta j_s(x_0, y_0) = j_c(x_0, y_0) \sin \phi(x_0, y_0)$ at I_c . To see this we write

$$\begin{aligned} \delta I_c &= I_{c,\text{on}} - I_{c,\text{off}} = \int (j_{s,\text{on}} - j_{s,\text{off}}) df \\ &= \int [j_c(T + \delta T) \sin \phi(T + \delta T) - j_c(T) \sin \phi(T)] df. \end{aligned} \quad (4)$$

Here, the subscripts “on” and “off” refer to electron beam switched on and off. The integral $\int (\dots) df$ has to be taken over the junction area A_j . The local j_c depends on the coordinates (x, y) via the Gaussian profile of $\delta T(x, y)$ and possible sample inhomogeneities. In addition, j_c is different in the 0 and π parts of the junction, with the values of j_c^0 and j_c^π at a given temperature. Assuming that the junction is small compared to λ_J and that a magnetic field B is applied in the (x, y) plane, with components B_x and B_y along x and y , the Josephson phase is given by the linear ansatz

$$\phi(x, y, \phi_0) = \phi_0 + (2\pi/\Phi_0) \cdot \Lambda(B_y x + B_x y). \quad (5)$$

At I_c the initial phase ϕ_0 is given such that the supercurrent is maximized. For junctions having electrode thicknesses larger than the London penetration depth λ_L , the effective junction thickness is $\Lambda \approx 2\lambda_L \approx d'$. For our Nb electrodes, using $\lambda_L = 90$ nm we estimate $\Lambda \approx 180$ nm. In general, the phase ϕ is different in the “on” and “off” states of the beam[43, 44]. When the electron beam disturbs the junction only slightly this difference may be neglected and we obtain

$$\delta I_c = \int \left[\frac{dj_c(x, y)}{dT} \cdot \sin \phi(x, y) \delta T(x - x_0, y_0) \right] df. \quad (6)$$

As can be seen in the lower right inset of Fig.1, at least for some of our junctions the normalized value

$$\left(\frac{dI_c}{dT} \frac{1}{I_c} \right)_{B=0} = \frac{dj_c}{dT} \frac{1}{j_c} \quad (7)$$

(assuming a homogeneous j_c^0, j_c^π) is about constant ($\approx -0.2 \text{ K}^{-1}$) and roughly the same for 0 and π parts. Note, however, that the latter statement, although valid for the junctions we study here, may not always be true. There are cases, *e.g.* near a temperature driven 0- π transition [10] where $(dj_c/dT)/j_c$ of 0 and π parts differ strongly in magnitude and perhaps even in sign. Assuming a constant value of $(dj_c/dT)/j_c$ we can further write

$$\delta I_c = \frac{dj_c}{dT} \frac{1}{j_c} \Delta T \langle j_s \rangle (x_0, y_0), \quad (8)$$

where we have used the notation

$$\langle j_s \rangle(x_0, y_0) = \int \left[j_c(x, y) \sin \phi(\phi_0, x, y) \frac{\delta T(x - x_0, y - y_0)}{\Delta T} \right] df, \quad (9)$$

where the brackets indicate the convolution of j_s with the beam-induced Gaussian temperature profile Eq. (3). When the size of the beam-induced perturbation is small compared to the structures to be imaged, we can approximate the Gaussian temperature profile with a δ -function, and further simplify the above expression to

$$\delta I_c \approx \frac{dj_c}{dT} \frac{1}{j_c} \Delta T j_c(x_0, y_0) \sin \phi(\phi_0, x_0, y_0) A_s, \quad (10)$$

with spot size $A_s \approx 2\pi\sigma^2$, defining an effective area under a 2D Gaussian distribution. Eq. (10) yields $\delta I_c \propto j_s(x_0, y_0) = j_c(x_0, y_0) \sin \phi(x_0, y_0)$. Thus, by monitoring δI_c , a map of j_s at I_c , including the supercurrent counterflow areas, can be obtained. Note, however, that in general the spot size is not small in comparison to the structures imaged. In particular, j_c sharply changes sign at a $0-\pi$ boundary. Thus, below, we use expression (9) to calculate images $\langle j_s \rangle(x_0, y_0)$ from the simulated supercurrent density $j_s(x, y)$ and compare them to the LTSEM images.

To obtain an LTSEM image we do not measure δI_c directly (the signal-to-noise ratio would be too small for reasonable measurement times which are limited by long term drifts) but bias the junctions slightly above its critical current at a given magnetic field and monitor the beam-induced voltage change $\delta V(x_0, y_0)$ as a function of the beam position (x_0, y_0) . To understand in more detail the corresponding response $\delta V(x_0, y_0)$ and the experimental requirements to produce a signal proportional to δI_c and thus proportional to j_s , we first note that at the operation temperature the $I-V$ characteristics can be described reasonably well by the RSJ model [45, 46],

$$V = \text{sgn}(I) \sqrt{I^2 - I_c(B)^2} / G \quad (11)$$

for $|I| > |I_c(B)|$ and $V = 0$ otherwise. Below we will always assume $I > 0$ and skip $\text{sgn}(I)$. Examples for a 0 reference junction are shown in Fig. 1. The $I-V$ characteristics have been recorded at $B = 0$ and at $B = 0.33$ mT, corresponding to the first side maximum of $I_c(B)$. Fits to the RSJ curve are shown by lines. Note that different values of G have been chosen for the two fits, which, in principle, is unphysical because G should not depend on B . In fact, if one fits these $I-V$ characteristics on a large scale one would get equal values of G ,

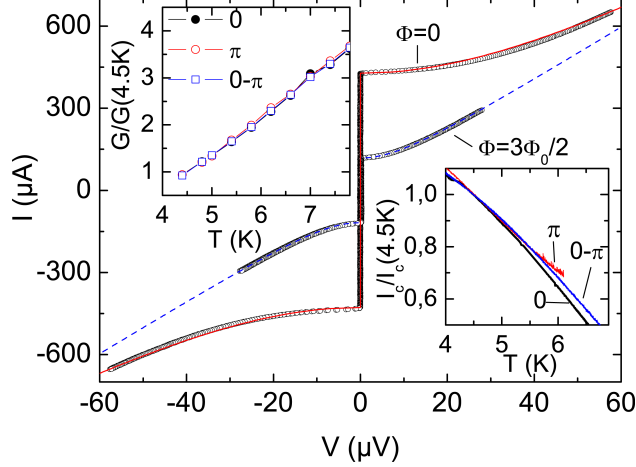


FIG. 1: (Color online) I - V characteristics of a reference 0 junction (#1 in Tab. I) at $T \approx 4.5$ K and applied magnetic flux $\Phi = 0$ and $3/2\Phi_0$, *i.e.* at the principal maximum and first side maximum of $I_c(B)$. Lines correspond to the RSJ curve (11), with $I_c = 428(118) \mu\text{A}$ and $G = 8.6(9.7) \Omega^{-1}$ for $\Phi = 0$ ($3/2\Phi_0$). Upper left inset shows normalized conductances $G/G(4.5\text{K})$ vs T for a 0, π and $0-\pi$ junction; $G(4.5\text{K}) \approx 9.5 \Omega^{-1}$ for the 0 and $0-\pi$ junction, and $\approx 9.3 \Omega^{-1}$ for the π junction. Lower right inset shows $I_c(T)$ at $\Phi = 0$, normalized to $I_c(4.5\text{K}) = 420, 170,$ and $124 \mu\text{A}$ for the 0, π , and $0-\pi$ junction, respectively. All junctions have dimensions of $10 \times 50 \mu\text{m}^2$.

however the region just above I_c will not be approximated well, because (11) is strictly valid only for $\beta_c \equiv 2\pi I_c R^2 C / \Phi_0 = 0$. In case of the I - V characteristic for $B = 0$ we estimate that $\beta_c \sim 0.5 \dots 0.8$. Therefore we adopt fits with field-dependent G to reproduce the I - V characteristics near I_c in the best way.

When scanning the beam over a junction, which is current-biased slightly above I_c , the changes δI_c and δG lead to a voltage change

$$\delta V = -\frac{\delta G}{G^2} \sqrt{I^2 - I_c(B)^2} - \frac{I_c(B) \delta I_c}{G \sqrt{I^2 - I_c(B)^2}}. \quad (12)$$

The change in G is related to the temperature rise caused by the electron beam. Similar to the case of the critical current, $\delta G(x_0, y_0) = \int df [(dG'/dT) \delta T(x - x_0, y - y_0)]$. The upper left inset of Fig.1 shows that the relative change $(dG/dT)/G = (dG'/dT)/G'$ is about constant for the junctions investigated, with a value of 0.75 K^{-1} . We, thus, can write $\delta G = (dG'/dT)/G' \cdot \int df [G'(x, y) \delta T(x - x_0, y - y_0)] \approx (dG'/dT)/G' \cdot G'(x_0, y_0) \Delta T A_s$. In general, $G'(x_0, y_0)$ is mainly set by the insulating Al_2O_3 layer and will not strongly differ for the 0 and π parts. Inserting expressions for δI_c and δG into (12) we find for the

beam-induced voltage change

$$\delta V = \frac{I_c(B)}{G} \frac{A_s}{A_j} \Delta T (F_I - F_G), \quad (13)$$

where

$$F_G = \frac{dG'}{dT} \frac{1}{G'} \frac{A_j G'(x_0, y_0)}{G} \sqrt{[I/I_c(B)]^2 - 1}, \quad (14)$$

and

$$F_I = -\frac{dj_c}{dT} \frac{1}{j_c} \frac{A_j j_c(x_0, y_0) \sin \phi(x_0, y_0)}{I_c(B) \sqrt{[I/I_c(B)]^2 - 1}}. \quad (15)$$

We emphasize here that these equations rely on the fact that Eq.(11) provides a good fit to the I - V characteristic in the region of interest and should at most be considered as semi-quantitative.

The response due to term F_G is parasitic, if one is interested in spatial variations of the supercurrent density. As $F_G > 0$, it will give a negative and, if spatial variations of $G'(x_0, y_0)$ are small, a basically constant contribution to δV for the whole junction area (*i.e.* a negative offset). F_I is the response of interest. To make $|F_I| \gg |F_G|$ one needs to satisfy the condition

$$\left| \left(\frac{dG'}{dT} \frac{1}{G'} \right) \left(\frac{dj_c}{dT} \frac{1}{j_c} \right)^{-1} \frac{A_j G'(x_0, y_0)}{G} \frac{I_c(B)}{A_j j_c(x_0, y_0) \sin \phi(x_0, y_0) G} \right| \ll \frac{1}{[I/I_c(B)]^2 - 1}. \quad (16)$$

When the conductance is about the same for 0 and π parts of the junction, $A_j G'(x_0, y_0)/G \approx 1$. Further, restricting requirement (16) to coordinates x_0, y_0 where $|\sin \phi(x_0, y_0)| \approx 1$ one obtains

$$\left| \left(\frac{dG'}{dT} \frac{1}{G'} \right) \left(\frac{dj_c}{dT} \frac{1}{j_c} \right)^{-1} \frac{I_c(B)}{A_j j_c(x_0, y_0)} \right| \ll \frac{1}{[I/I_c(B)]^2 - 1}, \quad (17)$$

with $|(dG'/dT)(1/G')(dj_c/dT)^{-1}j_c| \approx 3.75$ for our junctions (*cf.* insets of Fig.1). As we will see, when taking images at the maxima of $I_c(B)$, at least for $A_j j_c(x_0, y_0)/I_c(B) \approx 1$, Eq. (17) requires the bias current to be less than 10% above $I_c(B)$. Note, however, that there are cases where $A_j j_c(x_0, y_0)/I_c(B)$ is large, *e.g.*, for a homogeneous junction in high magnetic field or for a multi-facet junction when the supercurrents of the 0 and π segments almost cancel. In this case the F_G term is not dominant even much above I_c . On the other hand, to obtain a linear relation between δV and $j_s(x, y)$, I should be so far above I_c that $\sqrt{[I/I_c(B)]^2 - 1}$ varies only weakly when the beam is modulated. Typically, this requires I to be higher than about $1.05I_c(B)$, leaving only a small window to properly bias the junction, *i.e.* having a response $\delta V(x_0, y_0) \propto j_s(x_0, y_0)$.

III. RESULTS

In this section we discuss $I_c(B)$ patterns and LTSEM images of a variety of SIFS junctions. All data were obtained at $T \approx 4.5$ K. For reference, we will start with rectangular homogeneous 0 and π junctions and then turn to rectangular junctions consisting of two, three and forty 0 and π segments. Finally, we will discuss annular and disk shaped 0- π junctions. Sketches of the different geometries are shown as insets in figures 2(a) to 7(a).

A. Rectangular Junctions

For all rectangular junctions of length L and width W we use a coordinate system with its origin at the center of the junction, so that the barrier (at $z = 0$) spans from $-L/2$ to $+L/2$ in x direction and from $-W/2$ to $+W/2$ in y direction.

1. 0 and π Josephson junctions

We first discuss results obtained on a 0 junction (#1 in Tab. I). Fig. 2 shows $I_c(B)$ dependence, LTSEM images $\delta V(x, y)$ and corresponding line scans $\delta V(x)$ taken at $y = 0$. The left hand ordinate of Fig. 2(a) gives I_c in physical units while on the right hand ordinate we have I_c normalized to $I_{c0} = A_j j_c^0$. In the graph we compare $I_c(B)$ to the Fraunhofer dependence, $I_c(B) = I_c(0) |\sin \varphi / \varphi|$, with $\varphi = \pi B \Lambda L / \Phi_0$. In fact, having more complex structures in mind, rather than using the analytic expression, we have calculated the simulated curve in Fig. 2(a) as

$$I_c(B) = \max_{\phi_0} \int_{A_j} [j_c(x, y) \sin \phi(x, y, \phi_0)] df, \quad (18)$$

where $\phi(x, y, \phi_0)$ is a phase ansatz. Unless stated otherwise, we will assume a linear phase ansatz as given by Eq. (5). We note here that for junctions containing both 0 and π segments Λ may differ by some 5...10% in 0 and π regions[48, 49]. However, for the sake of simplicity, we ignore this effect here.

For the present junction we have used $j_c(x, y) = j_c^0 = const.$ The resulting calculated $I_c(B)$ curve, shown by the dashed line in Fig. 2(a), agrees with the experimental one, confirming the assumed homogeneity of j_c^0 . From the value of $I_c(0)$ we find $j_c^0 \approx 85$ A/cm² and $\lambda_J \approx 41$ μ m. Thus, the junction is in the short junction limit with $L/\lambda_J \approx 1.2$, justifying the

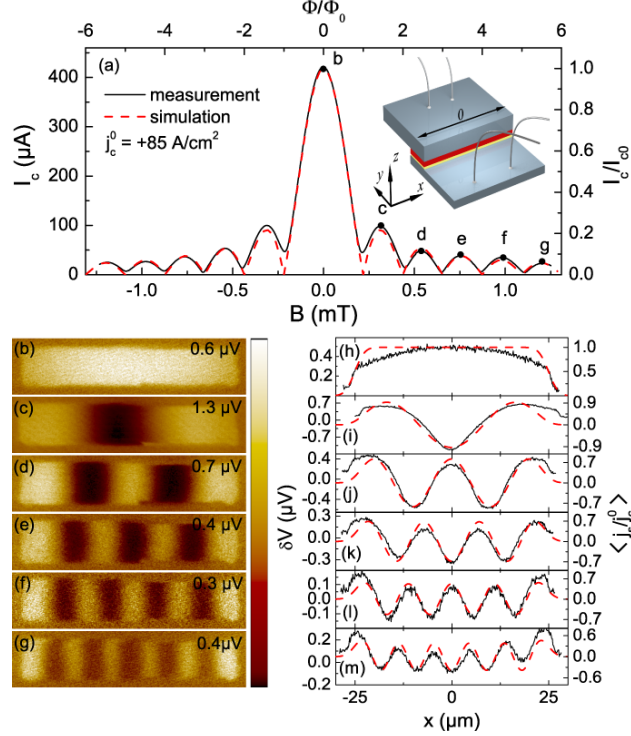


FIG. 2: (Color online). Φ_0 junction #1 in Tab. I: (a) $I_c(B)$ with $B \parallel y$. Solid (black) curve shows experimental data; dashed (red) curve is calculated using Eq. (18). Inset shows the junction geometry. (b)–(g) LTSEM images $\delta V(x, y)$ [47] taken at bias points indicated in (a). (h)–(m) line scans: solid (black) lines $\delta V(x)$ are extracted from the corresponding LTSEM images at $y = 0$; dashed (red) lines $\langle j_s \rangle(x)/j_c^0$ are calculated using a 1D version of Eq. (9).

use of the linear phase ansatz (5). Further, by comparing the abscissas of the experimental and simulated curves, one finds that $\Phi = \Phi_0$ corresponds to $B \approx 0.22$ mT. From this we obtain $\Lambda \approx 200$ nm in good agreement with the value of $\Lambda \approx 2\lambda_L \approx 180$ nm. Note that due to a magnetic field misalignment there will be a slight out-of-plane field component subject to flux focusing by large area superconducting films [50]. This leads to an increased value of Λ calculated using the above procedure.

Fig. 2(b) shows an LTSEM image at $B = 0$. The corresponding line scan is shown by the solid line in Fig.2(h). For $\delta V(x) \propto j_s(x) = j_c^0$ one would expect a constant response within the junction area. The actual response is somewhat smaller at the junction edges than in the interior. Taking the finite LTSEM resolution into account, *i.e.* calculating the convoluted supercurrent density distribution from Eq. (9), one obtains the dashed line which follows the measured response more closely, although there are still differences that

may be caused by the junction, either by a parabolic variation of j_c^0 or by a variation in conductance G' . To test this we implemented a parabolic variation of j_c^0 along x in the calculation of $I_c(B)/I_c(0)$ and found that the main effect is a slight reduction of the first side minima. To still be consistent with the measured $I_c(B)$ the variation should be well below 10% and is thus most likely not the origin of the δV variation. To discuss a potential G' effect we quantify the δV response using Eq. (13). For the image the bias current was set to $1.05I_c$. The function F_G amounts to 0.24 K^{-1} while for F_I we obtain 0.62 K^{-1} , *i.e.* changes in conductance contribute by about 1/3 to the total signal. Thus, variations of G' in principle could be responsible for the observed variation of δV . However, while we could accept a simple gradient of G' along x , the bending in δV which is symmetric with respect to the junction center, is hard to understand. We thus do not have a clear explanation for the parabolic shape of $\delta V(x)$. To quantify the LTSEM response further, we can look at its maximum value $\Delta V \approx 0.45 \mu\text{V}$. With $I_c/G \approx 50 \mu\text{V}$, from Eq. (13) one estimates $\Delta T A_s/A_j \approx 0.025 \text{ K}$ and from that a beam-induced temperature change $\Delta T \approx 0.2 \text{ K}$, which is somewhat less than 0.5 K estimated from beam-induced I_c changes.

Fig. 2(c) shows the LTSEM image taken at the first side maximum of $I_c(B)$. The field-induced sinusoidal variation of $\delta V(x)$ can nicely be seen. The corresponding line scan is shown by the solid line in Fig. 2(i) together with $\langle j_s \rangle(x)$, calculated using Eq. (9). Here, a potential parabolic-like variation of $\delta V(x)$, if present, would be overshadowed by the stronger field-induced variation. However, the sinusoidal variation of $\delta V(x)$ with an amplitude of $0.47 \mu\text{V}$ around an offset value of $-0.13 \mu\text{V}$ points to beam-induced changes in conductance. With the bias current $I = 1.1I_c(B)$ we find $F_G \approx 0.35/\text{K}$ and $F_I \approx -1.6/\text{K}$, *i.e.* we expect a 20% shift of the sinusoidal supercurrent-induced variation of δV towards lower voltages, roughly in agreement with observation. Further, from the modulation amplitude of $0.47 \mu\text{V}$ and $I_c/G = 12 \mu\text{V}$ we estimate $\Delta T A_s/A_j \approx 0.025 \text{ K}$ in agreement with the estimates for the zero field case.

Finally, Figs. 2(d)–(g) show LTSEM images and Figs. 2(j)–(m) corresponding line scans for higher order maxima in $I_c(B)$. In all cases, the field-induced modulation of $\delta V(x)$ can be seen clearly, and simulated curves for $\langle j_s \rangle(x)$, calculated using Eq. (9), are in good agreement with measurements.

We found similar results also for other reference junctions, including π ones. In the latter case, typical values at $T \approx 4.5 \text{ K}$ of the critical current densities are $j_c^\pi \sim 30 \text{ A/cm}^2$ (see *e.g.*

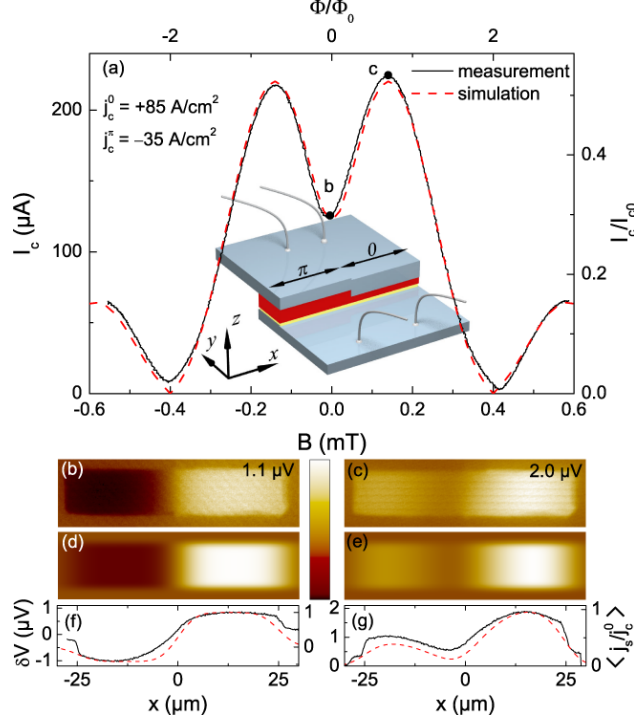


FIG. 3: (Color online). $0-\pi$ junction #3 in Tab. I: (a) $I_c(B)$ with $B \parallel y$. Solid (black) curve shows experimental data; dashed (red) curve is calculated using Eq. (18). Inset shows the junction geometry. (b),(c) LTSEM images $\delta V(x, y)$ [47] taken at bias points indicated in (a). (d),(e) corresponding images $\langle j_s \rangle(x, y)/j_c^0$ calculated using Eq. (9). (f),(g) line scans: solid (black) lines $\delta V(x)$ are extracted from the corresponding LTSEM images at $y = 0$; dashed (red) lines $\langle j_s \rangle(x)/j_c^0$ are calculated using a 1D version of Eq. (9).

#2 in Tab. I). This value is not large, but it is almost an order of magnitude higher than what has been previously reported for SIFS π junctions[16].

2. $0-\pi$ Josephson junction

Now we discuss data for a $0-\pi$ junction (#3 in Tab. I) presented in Fig. 3. The simulated $I_c(B)$ curve in Fig. 3(a) fits the experimentally measured dependence in the best way for $j_c^\pi/j_c^0 = -0.42$. The right hand axis is normalized to $I_{c0} = j_c^0 A_j$. From the measured value of $I_c(0)$ and the junction area A_j we find $j_c^0 = 85 \text{ A/cm}^2$ and $j_c^\pi = -35 \text{ A/cm}^2$. For a $0-\pi$ junction, λ_J can only be defined in 0 and π parts separately, but not for the junction as a whole. However, one can find a normalized junction length as

$$l \equiv \frac{L_0}{\lambda_J^0} + \frac{L_\pi}{\lambda_J^\pi}, \quad (19)$$

where L_0 and L_π are the total lengths of 0 and π parts and λ_J^0 and λ_J^π are the Josephson lengths in the 0 and π parts, respectively. With this definition we calculate $l \approx 1$, showing that the junction is again in the short limit. For Λ we obtain a reasonable value of 200 nm. Further note that the measured $I_c(B)$ is slightly asymmetric, *i.e.* the main maximum at negative field is slightly lower than at positive field. This effect, which is not reproduced by the simulated curve, is due to the finite magnetization of the F-layer which, in addition, is different in the 0 and π parts. This effect is addressed elsewhere[48].

For the 0- π junction, at $B=0$ the supercurrents of the two halves should have opposite sign. The part giving the smaller contribution to I_c should show inverse flow of supercurrent with respect to the applied bias current, *i.e.*, the π part in our case. This can be seen nicely in Fig. 3(b) showing an LTSEM $\delta V(x, y)$ image at zero field. The π part is on the left hand side. For comparison, Fig. 3(d) shows a $\langle j_s \rangle(x, y)/j_c^0$ image of the supercurrent density distribution, calculated using Eq. (9). For better comparison, Fig. 3(f) shows a measured and a calculated line scan. The left ordinate is shifted by $0.47 \mu\text{V}$ relative to the origin of the right ordinate to match the simulated and experimental curves. This shift is required to account for the beam-induced conductance change. More quantitatively, with $I/I_c(0) \approx 1.06$, $I_0/G = 13.5 \mu\text{V}$ and assuming that G' is the same for 0 and π parts, we estimate $F_G \approx 0.3 \text{K}^{-1}$. For the π part we estimate $F_I \approx -0.8 \text{K}^{-1}$, while for the 0 part we obtain $F_I \approx 1.9 \text{K}^{-1}$. The peak-to-peak voltage modulation in the LTSEM image is $1.65 \mu\text{V}$. From these numbers we estimate $(A_s/A_j)\Delta T \approx 0.045 \text{K}$, or $\Delta T \approx 0.3 \text{K}$, which is reasonable. For the conductance-induced shift we obtain a value of about $-0.2 \mu\text{V}$, which is about a factor of 2 less than expected from the measurement, but still within the error bars.

The LTSEM image $\delta V(x, y)$ shown in Fig. 3(c) has been taken at the main maximum of $I_c(B)$. Here, both parts of the junction give a positive response. The measurement is in good agreement with expectations, as can be seen in the calculated image $\langle j_s \rangle(x, y)/j_c^0$ in Fig. 3(e) and by comparing the line scans $\delta V(x)$ and $\langle j_s \rangle(x)/j_c^0$ shown in Fig. 3(g). Note that the ‘‘offset problem’’ seems to be less severe here. Indeed, with $I_c/G = 24 \mu\text{V}$ and $I/I_c = 1.019$ we obtain $F_G \approx 0.15 \text{K}^{-1}$ and $F_I \approx 2.1 \text{K}^{-1}$ for the 0 part and $F_I \approx 0.85 \text{K}^{-1}$ for the π part. The supercurrent term thus clearly dominates.

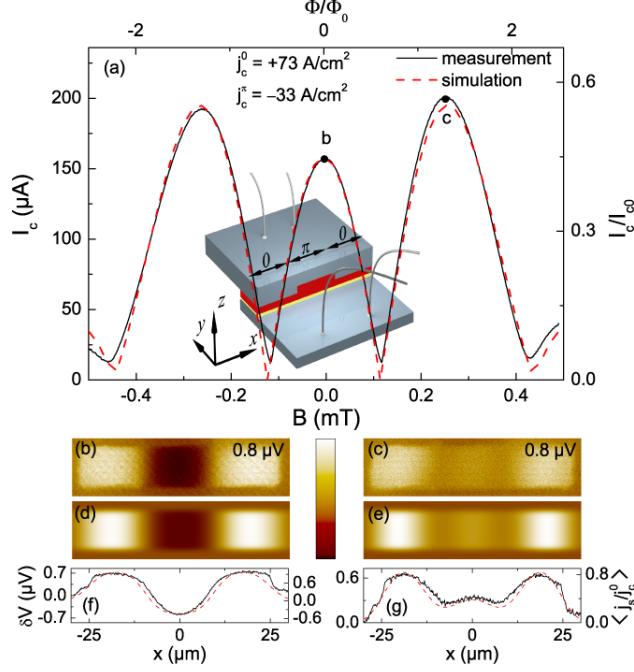


FIG. 4: (Color online). $0-\pi-0$ junction #4 in Tab. I: (a) $I_c(B)$ with $B \parallel y$. Solid (black) curve shows experimental data; dashed (red) curve is calculated using Eq. (18). Inset shows the junction geometry. (b),(c) LTSEM $\delta V(x,y)$ images[47] taken at bias points indicated in (a). (d),(e) corresponding images $\langle j_s \rangle(x,y)/j_c^0$ calculated using Eq. (9). (f),(g) line scans: solid (black) lines $\delta V(x)$ are extracted from the corresponding LTSEM images at $y = 0$; dashed (red) lines $\langle j_s \rangle(x)/j_c^0$ are calculated using a 1D version of Eq. (9).

3. $0-\pi-0$ Josephson junction

Next we discuss data for a $0-\pi-0$ junction (#4 in Tab. I) presented in Fig. 4. The best fit to $I_c(B)$ was obtained for $j_c^0 = 73 \text{ A/cm}^2$ and $j_c^\pi = -33 \text{ A/cm}^2$. From here we obtain ($l \approx 1$). We are thus again in the short junction limit. Further, we obtain $\Lambda \approx 200 \text{ nm}$.

LTSEM images, taken at, respectively, the central maximum and the main maximum at positive fields, are shown in Figs. 4(b) and (c). Figs. 4(d) and (e) are simulated images, and Figs. 4(f) and (g) show the corresponding line scans. For this junction, the simulated curves, taking only modulations due to j_s into account, agree well with the data. For Fig. 4(b), with $I/I_c = 1.044$ and $I_c/G = 17.5 \mu\text{V}$ we find $F_G \approx 0.22 \text{ K}^{-1}$ and, for the j_s maximum in the 0 part, $F_I^0 \approx 1.55 \text{ K}^{-1}$. For the j_s maximum in the π part we obtain $F_I^\pi \approx 0.7 \text{ K}^{-1}$. The offset is thus not very large. From the peak-to-peak modulation of

1.35 μV we estimate $(A_s/A_j)\Delta T \approx 0.035 \text{ K}$ and, thus, a reasonable value $\Delta T \approx 0.23 \text{ K}$. Taking this value, we estimate the offset voltage to about 0.1 μV . For the measurement at the main maximum with $I/I_c = 1.04$ we obtain $I_c/G = 23 \mu\text{V}$, $F_G \approx 0.21 \text{ K}^{-1}$, $F_I^0 \approx 1.29 \text{ K}^{-1}$ and $F_I^\pi \approx 0.58 \text{ K}^{-1}$. Using $(A_s/A_j)\Delta T = 0.035 \text{ K}$ we expect an offset in δV of $-0.17 \mu\text{V}$ and a maximum supercurrent response of 0.85 μV in the 0 parts, and 0.3 μV in the central π part. The measured numbers are 0.65 μV and 0.35 μV , respectively.

4. $20 \times (0-\pi-)$ Josephson junction

Having seen that well behaving 0- π -0 junctions can be fabricated one may consider multisegment structures where many 0- π segments are joined. The main purpose here is to check the complexity and reliability of the structures that can be fabricated already now. Moreover, as already mentioned in the introduction, multi-segment $N \times (0-\pi-)$ Josephson junctions are promising for the realization of a φ junction. The structure we study here has twenty 0- π segments (#5 in Tab. I). In Fig. 5(a) we compare the measured $I_c(B)$ dependence (solid line) with the one calculated (dashed line) using Eq. (18) with a linear phase ansatz (5). However, on both sides of each main peak we see quite substantial deviations of the calculated curve from the experimental one. In particular, the series of I_c maxima following the main peak are much higher in experiment than in simulations based on Eqs. (18) and (5). It is interesting that such a shape of $I_c(B)$ was also measured for d -wave/ s -wave zigzag shaped ramp junctions[32, 33, 34].

To understand the origin of such deviations, we have tested numerically a variety of local inhomogeneities $j_c(x)$ in the different facets, ranging from random scattering to gradients and parabolic profiles, always using the linear phase ansatz (5). None of them, and also no variations in effective junction thickness $\Lambda(x)$ were able to qualitatively reproduce the $I_c(B)$ features described above. Finally, it turned out that the quantity to be modified is the phase ansatz, *i.e.*, the field becomes non-uniform. Adding a cubic term, which accounts for a small phase bending, we have (assuming $B \parallel y$)

$$\phi(x, y, \phi_0) = \phi_0 + 2\pi \frac{B_y \Lambda L}{2\Phi_0} \left[\frac{2x}{L} + a_3 \left(\frac{2x}{L} \right)^3 \right]. \quad (20)$$

Calculating $I_c(B)$ using Eq. (18) with ϕ from Eq. (20), we were able to reproduce the above mentioned features of the experimental $I_c(B)$ dependence, as shown by the dotted line in

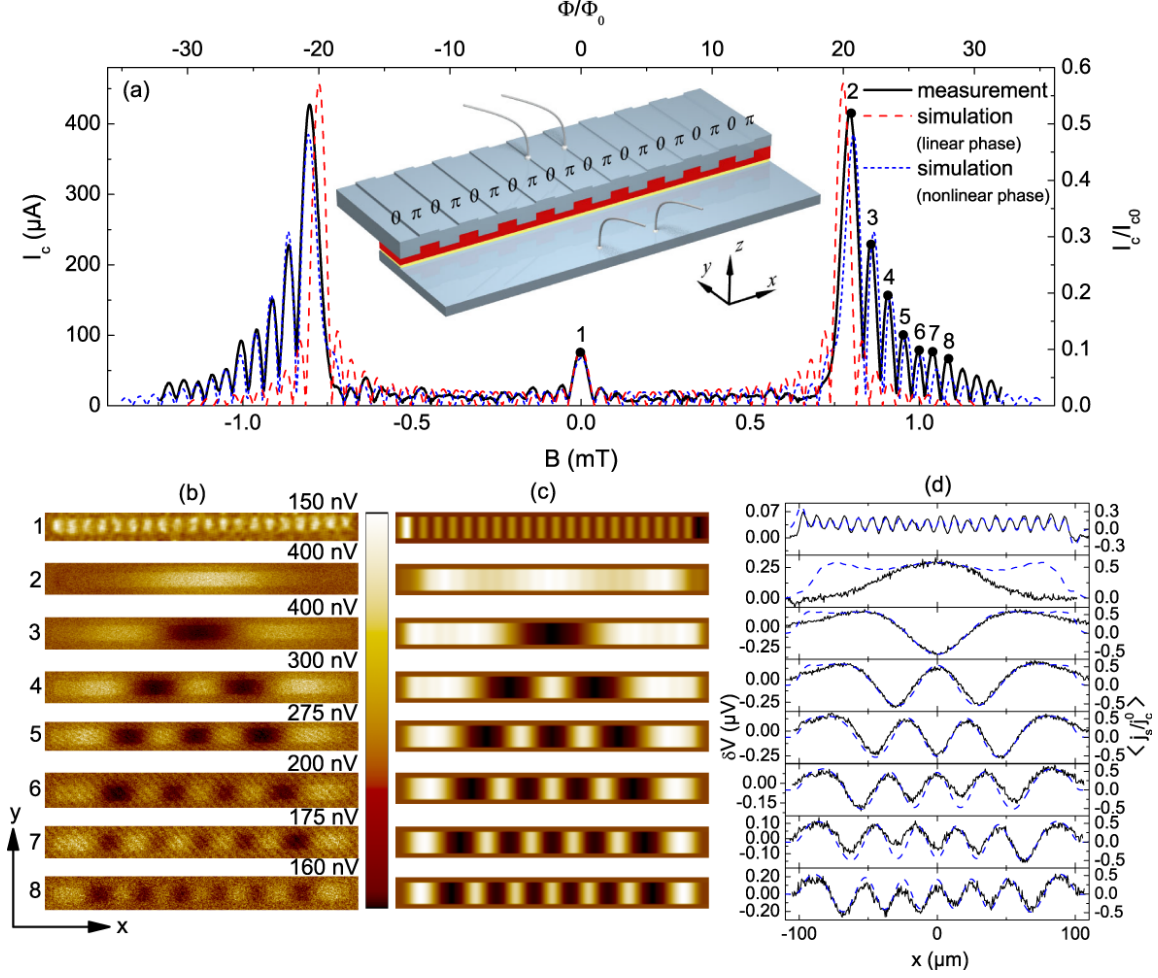


FIG. 5: (Color online). $20 \times (0-\pi-)$ junction #5 in Tab. I: (a) $I_c(B)$ with $B \parallel y$. Solid (black) curve shows experimental data; dashed (red) curve is calculated using Eq. (18) with linear phase ansatz (5); dotted (blue) curve is calculated using Eq. (18) with cubic phase ansatz (20). Inset shows the junction geometry. Only 10 $0-\pi-$ segments are drawn for simplicity. (b) LTSEM images $\delta V(x, y)$ [47] taken at the bias points indicated in (a) by numbers 1 to 8. (c) corresponding images $\langle j_s \rangle(x, y)/j_c^0$ calculated using Eq. (9) and the cubic phase ansatz (20). (d) line scans: solid (black) lines $\delta V(x)$ are extracted from the corresponding LTSEM images at $y = 0$; dashed (red) lines $\langle j_s \rangle(x)/j_c^0$ are calculated using Eq. (9).

Fig. 5(a). Here we used $a_3 = -0.065$, *i.e.* a rather small correction to the linear phase. In spite of this, for the relatively high magnetic fields around the main maxima of $I_c(B)$, this term adds up to an additional phase ~ 1 and becomes important — the contribution to the integral in Eq. (18) changes essentially close to the junction ends. Note that a homogeneous

junction or a junction consisting of only a few 0 and π segments could not sense that, since at the high fields, where the bending of the phase reaches values of ~ 1 at the junction edges, I_c is already suppressed to almost zero.

As we will show in a separate publication [49] the origin of the nonlinear contribution in Eq.(20) is a parasitic magnetic field component perpendicular to the junction plane, which appears due to a misalignment $\sim 1^\circ$ between the (x, y) plane and the applied magnetic field. This perpendicular component causes screening currents that result in a non-uniform (constant+parabolic) field focused inside the junction and pointing in y direction. Similar effects can also be present in non-local planar junctions[51], but we are far from this limit.

By comparing the nonlinear-phase simulation to the measured $I_c(B)$ we infer $j_c^0 = 37 \text{ A/cm}^2$, $j_c^\pi = -29.5 \text{ A/cm}^2$ and $l \approx 3$. The junction is thus still in the short limit. We further obtain $\Lambda \approx 350 \text{ nm}$, which is higher than the value we obtained for the other rectangular structures, but consistent with the fact that we have a focused out-of-plane field component.

Fig. 5(b) shows a series of LTSEM images. Image 1 is taken at $B = 0$, image 2 at the main maximum and images 3 to 8 at the subsequent maxima. For image 1 one can nicely see the modulation induced by the 40 facets, although negative signals are not reached any more. This is due to the small facet size of $5 \mu\text{m}$ which is on the LTSEM resolution limit. At the main maximum the signal is strong and positive, with a slight long-range modulation but no evidence of modulations due to the individual facets any more. At the higher maxima (images 3 to 8) additional minima appear in $\delta V(x, y)$. Fig. 5(c) shows the corresponding images calculated using the cubic phase ansatz, and Fig. 5(d) shows the corresponding line scans, comparing the measured $\delta V(x)$ (solid lines) with the calculated $\langle j_s \rangle(x)$ (dotted lines). As can be seen, the agreement is excellent, except for the line scan taken at the I_c maximum. Here, the measured response is strongly weakened towards the junction edges in contrast to the calculated modulation of j_s . For this bias, with $I = 1.029 I_c$ we estimate $F_G \approx 0.18 \text{ K}^{-1}$ and $F_I \approx 1.5 \text{ K}^{-1}$. It is thus not very likely that the discrepancy is caused by a spatially varying conductance. On the other hand, from the well behaved LTSEM images at zero field we can rule out a long range variation of j_c^0 and j_c^π as well. A possible origin of this behavior may be a non-uniform field focusing that results in a phase ansatz $\phi(x, y, \phi_0)$, which is more complicated than the cubic one of Eq. (20). However, we have to admit that we did not succeed in finding a proper dependence.

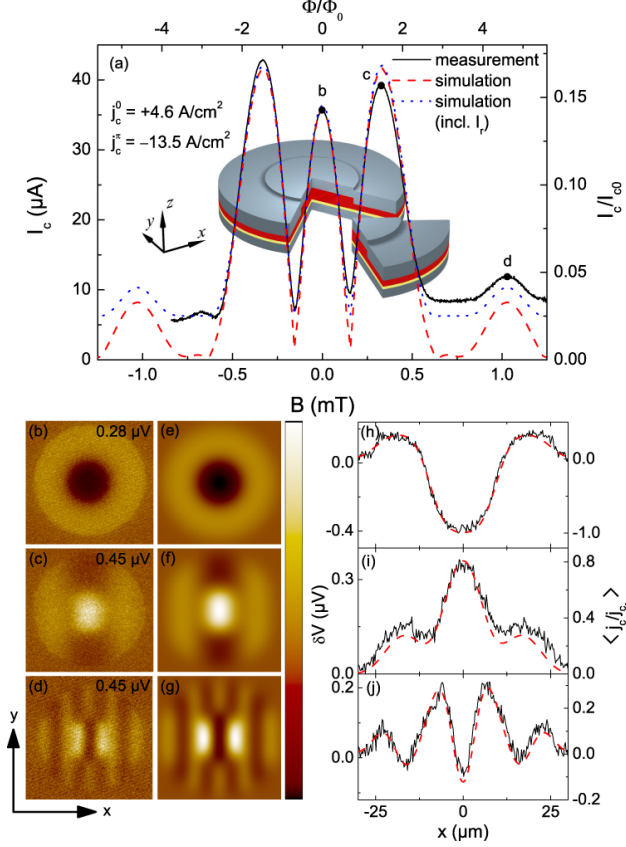


FIG. 6: (Color online). Disk shaped $0-\pi$ junction #6 in Tab. I: (a) $I_c(B)$ with $B \parallel y$. Solid (black) curve shows experimental data; dashed (red) curve is calculated using Eq. (18); dotted (blue) curve is calculated using Eq. (21). Inset shows the junction geometry. (b)–(d) LTSEM images $\delta V(x, y)$ [47] taken at bias points indicated in (a). (e)–(g) corresponding images $\langle j_s \rangle(x, y)/j_c^0$ calculated using Eq. (9). (h)–(j) line scans: solid (black) lines $\delta V(x)$ are extracted from the corresponding LTSEM images at $y = 0$; dashed (red) lines $\langle j_s \rangle(x)/j_c^0$ are calculated using Eq. (9).

We have measured several $20 \times (0-\pi)$ junctions. All behaved similar to the one discussed here, including the shape of $I_c(B)$ with a well developed set of maxima following the main peak and also with respect to LTSEM images. Thus, the present SIFS technology is fully able to deliberately produce quite complicated multi-facet $0-\pi$ junctions.

B. Disk Shaped and Annular Junctions

1. Disk shaped Josephson junction

The SIFS technology offers the possibility to create a more complex $0-\pi$ boundary than a linear one. An intriguing option is to close this boundary in a loop. The disk shaped junction #6 in Tab. I is of this type. Here, we use a coordinate system with its origin at the center of the disk, see the inset of Fig. 6(a). The $I_c(B)$ dependence, shown in Fig. 6(a), exhibits a central maximum at $B = 0$ where the critical currents of the 0 and the π part subtract, as well as prominent side maxima. By fitting the curve calculated using Eq. (18) (dashed line) to the experimental curve (solid line), we obtain $j_c^0 = 4.6 \text{ A/cm}^2$ and $j_c^\pi = -13.4 \text{ A/cm}^2$ as optimal fitting parameters. Referring to $2R$ as the junction length we obtain $l \approx 0.29$, *i.e.* again the junction is in the short limit. Fitting the horizontal axis using the length $2R$ we obtain $\Lambda \approx 200 \text{ nm}$.

For this sample, $I_c/G \approx 6.8 \mu\text{V}$ (at zero field) is rather low. As a consequence the detectability of $I_c(B)$ at low values of the critical current is resolution limited. We used a voltage criterion $V_{\text{cr}} = 1 \mu\text{V}$ to measure the “critical current”, yielding a parasitic I_c background of $I_r = V_{\text{cr}}G \approx 6 \mu\text{A}$. When comparing simulation with experiment the value of I_r should be added (in quadrature) to the calculated critical current I_c^{sim} to obtain the “visible critical current” I_c^{vis} , which should be compared with the experimental one I_c^{exp} , *i.e.*,

$$I_c^{\text{vis}} = \sqrt{(I_c^{\text{sim}})^2 + (I_r)^2}. \quad (21)$$

One can see in Fig. 6(a) that the calculated curve including I_r (dotted line) is in good agreement with the experimental data.

Fig. 6(b) shows an LTSEM image $\delta V(x, y)$ taken at the central maximum of $I_c(B)$. Fig. 6(e) shows the corresponding simulation of $\langle j_s \rangle(x, y)/j_c^0$ and Fig. 6(h) contains corresponding experimental and calculated line scans. The LTSEM data and the simulation results agree well, showing that the supercurrent in the central π region flows against the bias current. Figs. 6(c),(f),(i) show the results for an applied magnetic field corresponding to the first side maximum of the $I_c(B)$ curve. Here, the field-induced sinusoidal variation of the supercurrent is superimposed with the disk shaped $0-\pi$ variation. The supercurrents in the π region as well as in a major part of the 0 region flow in the direction of the bias current, maximizing I_c . For completeness, in Figs. 6(d),(g),(j) we also show corresponding

plots taken at the second side maximum of $I_c(B)$. Here, the magnetic field induces about 7 half oscillations of the supercurrent density along x . Similar to the previous cases, experimental and calculated plots agree well. For the central maximum with $I/I_c = 1.09$ we find $F_G \approx 0.3 \text{ K}^{-1}$ and $F_I^0 \approx 2.5 \text{ K}^{-1}$, $F_I^\pi \approx 7.2 \text{ K}^{-1}$. Thus, the offset due to conductance changes is minor in this case. The same holds for the other bias points. The main reason is that the factor $j_c(x_0, y_0)A_j/I_c(B)$ entering F_I is large (*e.g.* about 7 for the π part at $B = 0$).

2. Annular Josephson junction

The last structure we want to discuss in this paper is an annular 0- π junction (#7 in Tab. I, see the sketch in Fig. 7). Half of the ring is a 0 region and the other half is a π region. One thus obtains an annular junction with two 0- π boundaries. If the junction were long in units of λ_J it would be a highly interesting object to study (semi)fluxon physics, similar to the case of Nb junctions equipped with injectors[52, 53]. For this junction we use a coordinate system with its origin in the center of the ring, and the steps in the F-layer are located on the y axis. Fig. 7(a) shows $I_c(B)$ of this structure, with $B \parallel y$. The critical current is always above $10 \mu\text{A}$. This offset is in fact real and reproduced by the simulated $I_c(B)$ which is for $I_r = 0$ (the actual value $I_r \approx 8 \mu\text{A}$ only slightly lifts the $I_c(B)$ minima). From the fit we obtain a ratio $j_c^\pi/j_c^0 = -0.35$. Taking into account that $A_j \approx 1550 \mu\text{m}^2$, we get $j_c^0 \approx 7.3 \text{ A/cm}^2$ and $j_c^\pi \approx -2.5 \text{ A/cm}^2$ and, referring to the circumference as the junction length, $l \approx 3.5$. Thus, we are still in the short junction limit. Further, we obtain $\Lambda \approx 150 \text{ nm}$, which is somewhat lower than for the other junctions, but still reasonable.

Figures 7(b)–(e) show LTSEM images taken at various values of B as labeled in the $I_c(B)$ pattern shown in Fig. 7(a). As shown in Fig. 7(b) for $B = 0$, *i.e.* at the central local minimum in $I_c(B)$, a counterflow in the π part (left half) can be seen. At the main I_c maximum the supercurrents in both the 0 and the π region flow in the direction of bias current [Fig. 7(c)]. Images (d) and (e), taken at the subsequent $I_c(B)$ maxima, look more complicated, showing several regions of counterflow. In all cases, however, the LTSEM images are well reproduced by simulations, as can be seen in Figs. 7(f)–(i) and the corresponding linescans, see Figs. 7(j)–(m). The linescans, taken along the junction circumference, start at the upper 0- π boundary and continue clockwise.

For this annular junction we have also rotated the magnetic field by about 70° towards

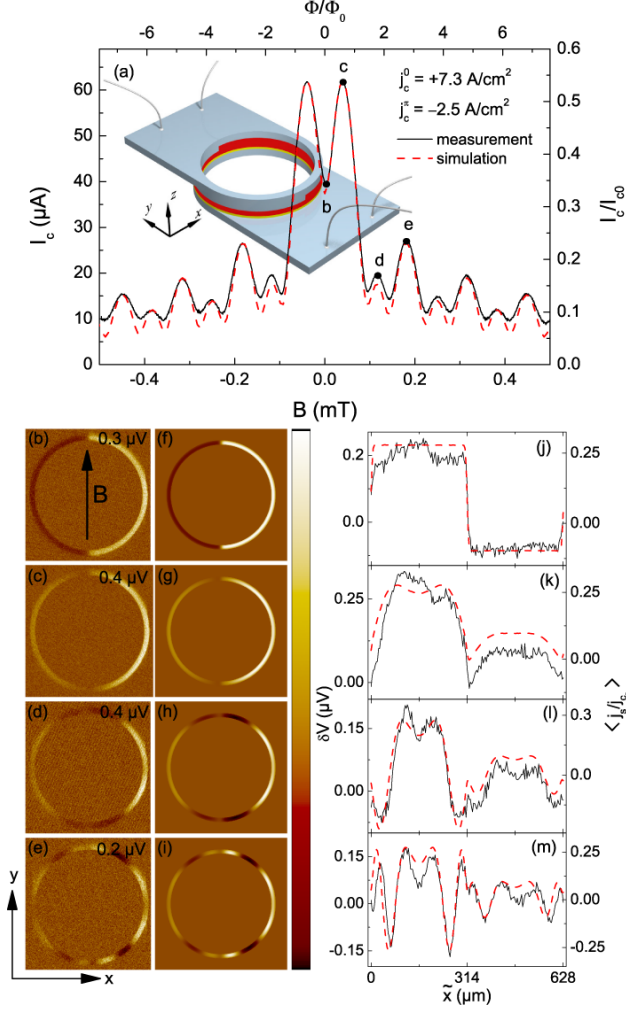


FIG. 7: (Color online). Annular $0-\pi$ junction #7 in Tab. I with $B \parallel y$: (a) $I_c(B)$ pattern; solid (black) curve shows experimental data; dashed (red) curve is calculated using Eq. (18). Inset shows the junction geometry. (b)–(e) LTSEM images[47] taken at bias points indicated in (a). (f)–(i) corresponding images calculated using Eq. (9). (g)–(m) line scans: solid (black) lines $\delta V(\tilde{x})$ are extracted from the corresponding LTSEM images; dashed (red) lines $\langle j_s \rangle(\tilde{x})/j_c^0$ are calculated using Eq. (9) with the curvilinear coordinate \tilde{x} instead of x which runs along the junction circumference.

the x direction. The corresponding data are shown in Fig. 8. For this field orientation $I_c(B)$ strongly differs from the case $B \parallel y$, *cf.*, Fig. 8(a), but can be reproduced by simulations, using the same j_c^0 and j_c^π as in Fig. 7. Furthermore, simulations show that if the field is rotated further towards the x axis, the height of the side maxima in $I_c(B)$ decreases, reaching only half of their height of the 70° case when the field is parallel to the x axis and the I_c minima reach zero. Thus, the annular $0-\pi$ junction reacts very sensitive to field

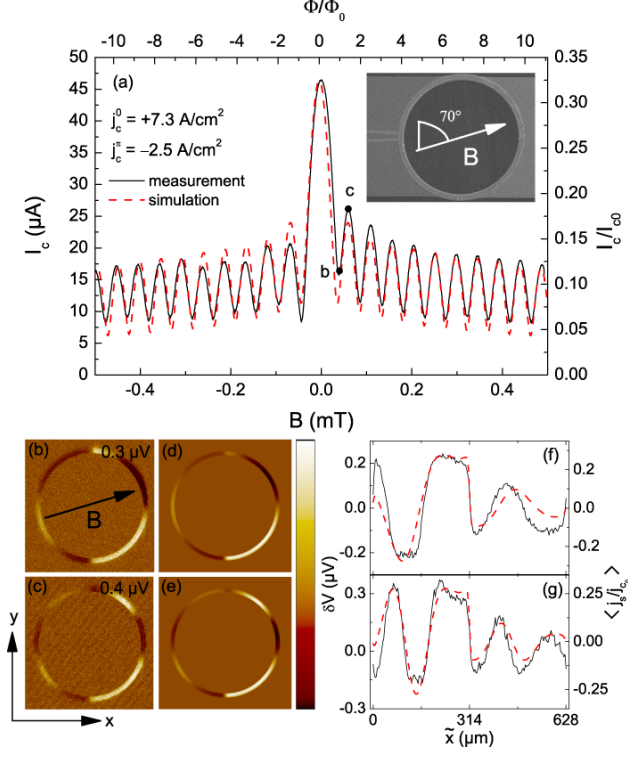


FIG. 8: (Color online). Annular $0-\pi$ junction #7 in Tab. I with B applied in the (x, y) plane under 70° from the y direction: (a) $I_c(B)$ pattern; solid (black) curve shows experimental data; dashed (red) curve is calculated using Eq. (18). Inset shows an SEM image of the junction. (b) and (c) LTSEM images[47] taken at bias points indicated in (a). (d) and (e) corresponding images calculated using Eq. (9). (f) and (g) line scans: solid (black) lines $\delta V(\tilde{x})$ are extracted from the corresponding LTSEM images; dashed (red) lines $\langle j_s \rangle(\tilde{x})/j_c^0$ are calculated using Eq. (9) for \tilde{x} .

misalignments relative to the x axis, similar to the case of the $20 \times (0-\pi-)$ junction where out-of-plane field components strongly altered $I_c(B)$. For completeness, Fig. 8(b)–(g) also shows LTSEM images taken at the selected bias points labeled in Fig. 8(a) and compare them with simulation. The agreement is again very good.

IV. CONCLUSION

We have studied a variety of SIFS Josephson junction geometries: rectangular 0 , π , $0-\pi$, $0-\pi-0$ and $20 \times (0-\pi-)$ junctions, disk-shaped $0-\pi$ junction, where the $0-\pi$ boundary forms a ring, and an annular junction with two $0-\pi$ boundaries. Using LTSEM we were able to image the supercurrent flow in these junctions and we demonstrate that 0 and π parts work

as predicted having $j_c^0 > 0$ and $j_c^\pi < 0$. Within each 0 or π part, according to both LTSEM images and $I_c(B)$, the critical current density is rather homogeneous. Particularly, within our experimental resolution of a few μm , we saw no inhomogeneities that might have been caused by an inhomogeneous magnetization of the F-layer. This implies that ferromagnetic domains, although probably present, must have a size well below $3 \mu\text{m}$.

These results demonstrate the capabilities of the state-of-the-art SIFS technology. Arrangements like the ring-shaped 0- π boundary are impossible to realize using other known 0- π junction technologies[30, 32, 33, 52]. Even intersecting 0- π boundaries seem to be feasible, *e.g.*, by arranging 0 and π segments in a checkerboard pattern.

For the π regions we demonstrated a record value of $j_c^\pi \approx 35 \text{ A/cm}^2$ at $T \approx 4.5 \text{ K}$, which is an order of magnitude higher than the values previously reported for SIFS junctions with a NiCu F-layer [16, 31]. Still, to obtain reasonable values of $\lambda_J \lesssim 20 \mu\text{m}$, j_c^π should be increased by at least one order of magnitude to reach $\sim 1 \text{ kA/cm}^2$. Then the 0- π junctions can be made long enough (in units of λ_J) to study the dynamics of semifluxons pinned at the 0- π boundaries. In this case semifluxon shapes, not realizable with other types of junctions, are possible, *e.g.*, closed loops, intersecting vortices, *etc.*. Another issue inherent to the present SIFS technology is that the critical current densities j_c^0 and j_c^π in the 0 and π parts are not identical in general. In many cases this does not matter, *e.g.*, when one works with semifluxons in a long junction. If $j_c^0 = |j_c^\pi|$ is required, the difference in j_c^0 and j_c^π will lead to a low yield of the circuit and one is perhaps restricted to operate the device in a narrow temperature interval, where j_c^0 and j_c^π are closer to each other.

Even with the present restrictions, quite complex geometries like the $20 \times (0-\pi)$ junctions have been realized. Those SIFS multifacet junctions already showed interesting features, like their high sensitivity to nonuniform magnetic fields, and they will be usable for many fundamental studies, *e.g.* on the way of realizing φ junctions.

Acknowledgments

We gratefully acknowledge financial support by the Deutsche Forschungsgemeinschaft via SFB/TRR-21 and project WE 4359/1-1, and by the German Israeli Foundation via research

grant G-967-126.14/2007.

- [1] L. N. Bulaevskii, V. V. Kuzii, and A. A. Sobyenin, *JETP Lett.* **25**, 290 (1977).
- [2] E. Terzioglu, D. Gupta, and M. R. Beasley, *IEEE Trans. Appl. Supercond.* **7**, 3642 (1997).
- [3] E. Terzioglu and M. R. Beasley, *IEEE Trans. Appl. Supercond.* **8**, 48 (1998).
- [4] A. V. Ustinov and V. K. Kaplunenko, *J. Appl. Phys.* **94**, 5405 (2003).
- [5] T. Ortлеpp, Ariando, O. Mielke, C. J. M. Verwijs, K. F. K. Foo, H. Rogalla, F. H. Uhlmann, and H. Hilgenkamp, *Science* **312**, 1495 (2006).
- [6] L. B. Ioffe, V. B. Geshkenbein, M. V. Feigel'man, A. L. Fauchère, and G. Blatter, *Nature (London)* **398**, 679 (1999).
- [7] G. Blatter, V. B. Geshkenbein, and L. B. Ioffe, *Phys. Rev. B* **63**, 174511 (2001).
- [8] T. Yamashita, K. Tanikawa, S. Takahashi, and S. Maekawa, *Phys. Rev. Lett.* **95**, 097001 (2005).
- [9] T. Yamashita, S. Takahashi, and S. Maekawa, *Appl. Phys. Lett.* **88**, 132501 (2006).
- [10] V. V. Ryazanov, V. A. Oboznov, A. Y. Rusanov, A. V. Veretennikov, A. A. Golubov, and J. Aarts, *Phys. Rev. Lett.* **86**, 2427 (2001).
- [11] T. Kontos, M. Aprili, J. Lesueur, F. Genet, B. Stephanidis, and R. Boursier, *Phys. Rev. Lett.* **89**, 137007 (2002).
- [12] Y. Blum, A. Tsukernik, M. Karpovski, and A. Palevski, *Phys. Rev. Lett.* **89**, 187004 (2002).
- [13] A. Bauer, J. Bentner, M. Aprili, M. L. Della-Rocca, M. Reinwald, W. Wegscheider, and C. Strunk, *Phys. Rev. Lett.* **92**, 217001 (2004).
- [14] H. Sellier, C. Baraduc, F. Lefloch, and R. Calemczuk, *Phys. Rev. Lett.* **92**, 257005 (2004).
- [15] V. A. Oboznov, V. V. Bolginov, A. K. Feofanov, V. V. Ryazanov, and A. I. Buzdin, *Phys. Rev. Lett.* **96**, 197003 (2006).
- [16] M. Weides, M. Kemmler, E. Goldobin, D. Koelle, R. Kleiner, H. Kohlstedt, and A. Buzdin, *Appl. Phys. Lett.* **89**, 122511 (2006).
- [17] O. Vavra, S. Gazi, D. S. Golubovic, I. Vavra, J. Derer, J. Verbeeck, G. VanTendeloo, and V. V. Moshchalkov, *Phys. Rev. B* **74**, 020502(R) (2006).
- [18] A. A. Bannykh, J. Pfeiffer, V. S. Stolyarov, I. E. Batov, V. V. Ryazanov, and M. Weides, *Phys. Rev. B* **79**, 054501 (2009).

- [19] J. A. van Dam, Y. V. Nazarov, E. P. A. M. Bakkers, S. D. Franceschi, and L. P. Kouwenhoven, *Nature (London)* **442**, 667 (2006).
- [20] J.-P. Cleuziou, W. Wernsdorfer, V. Bouchiat, T. Ondarcuhu, and M. Monthieux, *Nature Nanotech.* **1**, 53 (2006).
- [21] H. Jorgensen, T. Novotny, K. Grove-Rasmussen, K. Flensberg, and P. Lindelof, *Nano Lett.* **7**, 2441 (2007).
- [22] J. J. A. Baselmans, A. F. Morpurgo, B. J. V. Wees, and T. M. Klapwijk, *Nature (London)* **397**, 43 (1999).
- [23] J. J. A. Baselmans, B. J. van Wees, and T. M. Klapwijk, *Phys. Rev. B* **65**, 224513 (2002).
- [24] J. Huang, F. Pierre, T. T. Heikkilä, F. K. Wilhelm, and N. O. Birge, *Phys. Rev. B* **66**, 020507(R) (2002).
- [25] L. N. Bulaevskii, V. V. Kuzii, and A. A. Sobyenin, *Solid State Commun.* **25**, 1053 (1978).
- [26] J. H. Xu, J. H. Miller, and C. S. Ting, *Phys. Rev. B.* **51**, 11958 (1995).
- [27] E. Goldobin, D. Koelle, and R. Kleiner, *Phys. Rev. B* **66**, 100508(R) (2002).
- [28] J. R. Kirtley, C. C. Tsuei, M. Rupp, J. Z. Sun, L. S. Yu-Jahnes, A. Gupta, M. B. Ketchen, K. A. Moler, and M. Bhushan, *Phys. Rev. Lett.* **76**, 1336 (1996).
- [29] J. R. Kirtley, C. C. Tsuei, and K. A. Moler, *Science* **285**, 1373 (1999).
- [30] H. Hilgenkamp, Ariando, H. H. Smilde, D. H. A. Blank, G. Rijnders, H. Rogalla, J. Kirtley, and C. C. Tsuei, *Nature (London)* **422**, 50 (2003).
- [31] M. Weides, M. Kemmler, H. Kohlstedt, R. Waser, D. Koelle, R. Kleiner, and E. Goldobin, *Phys. Rev. Lett.* **97**, 247001 (2006).
- [32] H.-J. H. Smilde, Ariando, D. H. A. Blank, G. J. Gerritsma, H. Hilgenkamp, and H. Rogalla, *Phys. Rev. Lett.* **88**, 057004 (2002).
- [33] Ariando, D. Darminto, H. J. H. Smilde, V. Leca, D. H. A. Blank, H. Rogalla, and H. Hilgenkamp, *Phys. Rev. Lett.* **94**, 167001 (2005).
- [34] C. Gürlich, E. Goldobin, R. Straub, D. Doenitz, Ariando, H.-J. H. Smilde, H. Hilgenkamp, R. Kleiner, and D. Koelle, *Phys. Rev. Lett.* **103**, 067011 (2009).
- [35] J. Mannhart, H. Hilgenkamp, B. Mayer, C. Gerber, J. R. Kirtley, K. A. Moler, and M. Sgrist, *Phys. Rev. Lett.* **77**, 2782 (1996).
- [36] A. Buzdin and A. E. Koshelev, *Phys. Rev. B.* **67**, 220504(R) (2003).
- [37] E. Goldobin, D. Koelle, R. Kleiner, and A. Buzdin, *Phys. Rev. B* **76**, 224523 (2007).

- [38] R. G. Mints, Phys. Rev. B **57**, R3221 (1998).
- [39] R. G. Mints and I. Papiashvili, Phys. Rev. B **64**, 134501 (2001).
- [40] R. G. Mints, I. Papiashvili, J. R. Kirtley, H. Hilgenkamp, G. Hammerl, and J. Mannhart, Phys. Rev. Lett. **89**, 067004 (2002).
- [41] R. Gross and D. Koelle, Rep. Prog. Phys. **57**, 651 (1994).
- [42] M. Weides, C. Schindler, and H. Kohlstedt, J. Appl. Phys. **101**, 063902 (2007).
- [43] J. J. Chang and D. J. Scalapino, Phys. Rev. B. **29**, 2843 (1984).
- [44] J. J. Chang, C. H. Ho, and D. J. Scalapino, Phys. Rev. B. **31**, 5826 (1985).
- [45] W. C. Stewart, Appl. Phys. Lett. **12**, 277 (1968).
- [46] D. McCumber, J. Appl. Phys. **39**, 3113 (1968).
- [47] The color scale of all images is symmetric around zero, with the maximum values given on each image.
- [48] M. Kemmler, M. Weides, M. Weiler, T. B. Goennenwein, A. S. Vasenko, A. A. Golubov, H. Kohlstedt, D. Koelle, R. Kleiner, and E. Goldobin, arXiv:0910.5907 (2009).
- [49] S. Scharinger, C. Gürlich, M. Weides, R. G. Mints, H. Kohlstedt, D. Koelle, R. Kleiner, and E. Goldobin, unpublished (2009).
- [50] M. B. Ketchen, W. J. Gallagher, A. W. Kleinsasser, S. M. S, and J. R. Clem, Proc. SQUID85, Superconducting Quantum Interference Devices and their Applications ed. H. D. Hahlbohm and H. Lübbig (Berlin: Walter de Gruyter) p. 865 (1985).
- [51] M. Moshe, V. G. Kogan, and R. G. Mints, Phys. Rev. B. **79**, 024505 (2009).
- [52] E. Goldobin, A. Sterck, T. Gaber, D. Koelle, and R. Kleiner, Phys. Rev. Lett. **92**, 057005 (2004).
- [53] U. Kienzle, T. Gaber, K. Buckenmaier, K. Ilin, M. Siegel, D. Koelle, R. Kleiner, and E. Goldobin, Phys. Rev. B. **80**, 014504 (2009).